

Shape transition and coexistence in Te isotopes studied with the quadrupole collective Hamiltonian based on a relativistic energy density functional

K. Suzuki¹ and K. Nomura^{1,2,*}

¹*Department of Physics, Hokkaido University, Sapporo 060-0810, Japan*

²*Nuclear Reaction Data Center, Hokkaido University, Sapporo 060-0810, Japan*

(Dated: December 6, 2024)

Evolution and coexistence of shape and the related spectroscopic properties of even-even Te isotopes are investigated within the quadrupole collective model that is based on the nuclear density functional theory. By means of the constrained self-consistent mean-field calculations performed within the relativistic Hartree-Bogoliubov method with a choice of the energy density functional and pairing interaction, the deformation-dependent mass parameters and moments of inertia as well as collective potential of the triaxial quadrupole collective Hamiltonian are completely determined. The collective model produces for the near mid-shell nuclei, e.g., ¹¹⁶Te and ¹¹⁸Te, the low-energy 0_2^+ state, which can be interpreted as the intruder state originating from the strongly deformed prolate minimum in the potential energy surface, along with the 0_1^+ ground state that is attributed to the normal state based on a weakly oblate deformed global minimum. The collective model calculation suggests a parabolic behavior of the 0_2^+ energy level near the neutron mid-shell $N = 66$, as observed experimentally. Sensitivities of the calculated low-energy spectra to the pairing strength and collective mass parameters are analyzed.

I. INTRODUCTION

The atomic nucleus is a composite system of neutrons and protons, where a subtle interplay between single-particle and collective motions plays a crucial role. Remarkable features of the nucleus are the fact that it organizes itself into a variety of shapes, and that the related collective excitations such as the anharmonic vibrations of the nuclear surface and rotational motions emerge [1]. The dominant nuclear deformation is of quadrupole type, which is characterized by the axial deformation β , i.e., degree of elongation along the symmetry axis of an ellipsoid, and the nonaxial or triaxial deformation γ , representing the deviation from the axial symmetry. Different values of the γ deformation correspond to the prolate ($\gamma = 0^\circ$), oblate ($\gamma = 60^\circ$), and γ -soft ($0^\circ < \gamma < 60^\circ$) shapes.

The nuclear structure undergoes a transition from a nearly spherical vibrational to deformed rotational states when it is seen as a function of the neutron number N or proton Z number. Such a nuclear structural evolution often takes place quite rapidly at a particular nucleon number, and is considered a quantum phase transition [2], which is observable from striking differences of the measured intrinsic and spectroscopic properties between neighboring nuclei. In addition, several different nuclear shapes can coexist especially for those nuclei near the magic numbers, and several excited 0^+ levels appear that are close in energy to the ground state [3–6]. The phenomenon of shape coexistence was found experimentally in the light mass region, i.e., ¹⁶O [7], and later was identified in heavy nuclei as well, a representative example being the spherical-oblate-prolate triple shape coexistence in ¹⁸⁶Pb [8], hence it is nowadays considered to be a uni-

versal feature observed in a wide spectrum of the chart of nuclides (see Ref. [6] for a recent review).

An interpretation of the shape coexistence is given by the spherical shell model: particularly for those nuclei that are near shell closure, multiparticle-multiparticle excitations are likely to occur, and they enhance correlations between valence neutrons and protons, which can be strong enough to substantially lower the non-yrast 0^+ states to be in the vicinity of the ground state 0_1^+ [3–5, 9–11]. The different shell-model configurations are in the mean-field language related to several minima of the potential energy surface defined in the relevant collective coordinates. In the mean-field model calculations, several local minima that are rather close in energy to the global minimum often appear, and they are considered a signature of shape coexistence [4, 5, 8, 12–14].

Evidence for shape coexistence and the well established intruder bands built on the low-lying excited 0_2^+ state are most spectacularly observed in those nuclei in the neutron-deficient Hg-Pb regions, where the proton two-quasiparticle $\pi(h_{9/2})^2$ and four-quasiparticle $\pi(h_{9/2})^4$ excitations are likely to occur near the mid-shell $N = 104$. A similar mechanism could play a role in the low-lying states of those isotopes near the $Z = 50$ major shell closure, including Cd ($Z = 48$), Sn ($Z = 50$), Te ($Z = 52$), etc. isotopes. These nuclei were regarded as a textbook example for the anharmonic vibrator based on the multiphonon picture. In the case of the Cd isotopes, however, more recent experiments revealed additional low-spin levels near the multiphonon multiplets, and these new state could not be accounted for without introducing the contributions of the shape coexistence or intruder states coming from the next major oscillator shell. In the Sn as well as Cd isotopes, much experimental evidence has been found for the presence of the low-lying intruder band built on the 0_2^+ state and its parabolic tendency toward the neutron mid-shell $N = 66$ (see Ref. [6], and

* nomura@sci.hokudai.ac.jp

references are therein).

It is then expected that the shape coexistence may play a role in Te isotopes with $Z = 52$, as they are also close to the $Z = 50$ magic number and the cross-shell excitations of the intruder orbitals could be relevant in low-lying states. Existence of intruder states in low-energy spectra of the even-even $^{116-128}\text{Te}$ nuclei was pointed out by an earlier experimental study of Ref. [15]. Lifetime measurements were performed for revealing a detailed level structure of ^{118}Te [16]. In recent years more and more experimental studies have been made to identify the intruder states and shape coexistence in near mid-shell Te isotopes. An experiment at the Cologne FN Tandem accelerator found several new low-energy levels in ^{116}Te [17]. The latter two experimental studies, i.e., [16, 17], point to the possible occurrence of the shape coexistence in the mid-shell Te isotopes, whereas the theoretical interpretation used in those references was based on a simple interacting boson model (IBM) [18] calculation, which did not take into account contributions from the intruder configuration, and in which the model parameters were fit to data. In addition, a lifetime measurement has recently been made investigating the 2_1^+ energy and $B(E2; 0_1^+ \rightarrow 2_1^+)$ transition of ^{118}Te [19]. The same quantities for the ^{116}Te and ^{118}Te nuclei, together with their systematic trends along the entire Te isotopic chain in the neutron $N = 50 - 82$ major shell were studied through another lifetime measurement, in comparison with the large-scale shell model calculations [20]. Several other experiments on the Te nuclei with $N \geq 68$ have been performed in recent decades. For further details and the relevant references, the reader is referred to Ref. [6]. Much more experimental information is still required, in order to identify the evidence for shape coexistence and intruder bands in Te isotopes as firmly as in the case of the Sn and Cd isotopes, and this also necessitates systematic theoretical studies to be made in a timely manner.

From a theoretical point of view, low-energy excitation spectra and electromagnetic transition rates that signal the shape coexistence in the Te isotopes in open shell region have been carried out from various perspectives, e.g., the nuclear shell model [20–23], the static [24, 25] and beyond [26–29] self-consistent mean-field (SCMF) models based on the nuclear energy density functional (EDF), the IBM [15–17, 30–33], the geometrical collective model [34] and an effective field theory [35]. The SCMF method, in particular, that employs a given nonrelativistic (e.g., Skyrme [36–38] and Gogny [39, 40]) or relativistic [41, 42] EDF is among the most reliable theoretical tools able to give a universal description of the nuclear matter properties, the intrinsic properties of finite nuclei including masses, radii, and deformations, and the low-energy collective excitations. To compute energies and wave functions of the excited states, the EDF framework needs to be extended to include dynamical correlations that are beyond the mean-field approximations, which are associated with the broken symmetries and with the quan-

tum fluctuations around the mean-field minimum. It is then necessary to project mean-field solutions onto states with good symmetry quantum numbers and perform configuration mixing [43]. The beyond-mean-field treatment is made in principle by means of the generator coordinate method (GCM) [37, 40, 43]. The GCM approach is, however, often computationally demanding for heavy nuclei, especially when the quadrupole triaxial or other higher-order shape degrees of freedom should be considered as collective coordinates. More computationally feasible EDF-based approaches to nuclear collective excitations are provided by solving the five-dimensional quadrupole collective Hamiltonian (QCH) [28, 42, 44], and by mapping the mean-field potential energy surface (PES) onto the IBM Hamiltonian [45–47].

In the present article, by using the theoretical framework of the QCH that is based on the relativistic EDF, we study the low-energy collective states along the Te isotopic chain, and investigate possible shape coexistence around the neutron mid-shell $N = 66$. Here the parameters of the QCH are completely determined by the constrained SCMF calculation employing given relativistic EDFs and pairing interactions. Over the last two decades the QCH within the relativistic EDF framework [42, 44, 48] has found a number successful applications in describing various nuclear properties in different mass regions, including the shape coexistence (see, e.g., [49–52]), and quantum phase transitions (see, e.g., [42, 48, 53–55]), and is thus considered a sensible microscopic approach to nuclear low-lying collective states. In particular, the same approach has recently been applied to study a shape phase transition and critical-point symmetry in the Kr isotopes below $N = 82$ [55], and the shape coexistence and intruder states in the Cd isotopes [52]. Here we extend the previous EDF-based QCH calculation for the Cd isotopes [52] to study low-lying states and physical quantities that indicate the relevance of shape coexistence along the chain of the Te isotopes, and give a timely theoretical description of the spectroscopic properties of those Te nuclei that are becoming of much interest experimentally. In addition, as a possible source of model uncertainty we further investigate the sensitivity of the results on relevant building blocks of the employed model, specifically, the pairing correlations considered in the SCMF model, and the collective mass parameters of the QCH.

This article is organized as follows. We briefly describe our theoretical framework in Sec. II. The mean-field results are presented in Sec. III, and the QCH results for the spectroscopic properties are discussed in Sec. IV. Section V gives a summary of the main results and concluding remarks.

II. THEORETICAL FRAMEWORK

The first step of our theoretical analysis is to perform, for each Te nucleus, a set of the constrained SCMF

calculations within the framework of the relativistic Hartree-Bogoliubov (RHB) method [41, 42, 56, 57]. For the particle-hole channel, we employ two representative classes of the relativistic EDF: density-dependent point-coupling (DD-PC1) [58] and density-dependent meson-exchange (DD-ME2) [59] interactions. Note, however, that since the results obtained from both EDFs are similar to each other, we mainly discuss in this paper the DD-PC1 results. For the particle-particle channel, we consider the separable pairing force of finite range that was developed in Ref. [60], given in coordinate space as

$$V(\mathbf{r}_1, \mathbf{r}_2, \mathbf{r}'_1, \mathbf{r}'_2) = -V\delta(\mathbf{R} - \mathbf{R}')P(\mathbf{r})P(\mathbf{r}')\frac{1}{2}(1 - P^\sigma), \quad (1)$$

where $\mathbf{R} = (\mathbf{r}_1 + \mathbf{r}_2)/2$ and $\mathbf{r} = \mathbf{r}_2 - \mathbf{r}_1$ are the center-of-mass and relative coordinates, respectively. The factor $P(\mathbf{r})$ takes the form of a Gaussian function,

$$P(\mathbf{r}) = \frac{1}{(4\pi a^2)^{3/2}} e^{-\mathbf{r}^2/4a^2}. \quad (2)$$

The strength parameter $V = 728 \text{ MeV fm}^3$ and the other parameter $a = 0.644 \text{ fm}$ were fixed in Ref. [60], so that the 1S_0 pairing gap of infinite nuclear matter resulting from the Hartree-Fock-Bogoliubov (HFB) model calculation using the Gogny-D1S EDF [61] should be reproduced.

The sensitivity of the mean-field results on the strength of the separable pairing force was systematically analyzed in Ref. [62], and it was suggested that the pairing strength V in Eq. (1) may vary as functions of nucleon number in order to account for the empirical odd-even mass staggering in medium-heavy and heavy nuclei. V should be subject to be modified as $V \rightarrow V' = fV$, with f being a scaling factor. In the present study, we consider the default pairing strength with $f = 1.0$ and the value increased by 5% of V , corresponding to $f = 1.05$. We further adopt a type of the factor that takes into account the neutron-proton number difference, i.e.,

$$f(N) = c_1 \exp\left(c_2 \frac{|N - Z|}{A}\right), \quad (3)$$

with c_1 and c_2 being parameters. The above form (3) was considered in Ref. [62], and was shown to gradually decrease along an isotopic chain. In all these three cases of the pairing strength, we consider equal values for the neutron and proton pairings, as in Ref. [60]. The parameters $c_1 = 1.1$ and $c_2 = -0.58$ are here chosen, so as to fulfill the conditions that they are more or less similar to those values typically considered in Ref. [62], and that the factor f varies along the isotopic chain from 1.1 ($N = 52$) to 0.97 ($N = 80$), leading to an overall agreement with the experimental 2^+_1 level on both ends of the isotopic chain, i.e., at $N \approx 54$ and $N \approx 78$.

The constraints imposed in the SCMF calculations are on the expectation values of the mass quadrupole operators

$$\hat{Q}_{20} = 2z^2 - x^2 - y^2 \quad \text{and} \quad \hat{Q}_{22} = x^2 - y^2, \quad (4)$$

which are related to the axially symmetric deformation β and triaxiality γ [1], through the relations

$$\beta = \sqrt{\frac{5}{16\pi}} \frac{4\pi}{3} \frac{1}{A(r_0 A^{1/3})^2} \sqrt{\langle \hat{Q}_{20} \rangle^2 + 2\langle \hat{Q}_{22} \rangle^2}, \quad (5)$$

$$\gamma = \arctan \sqrt{2} \frac{\langle \hat{Q}_{22} \rangle}{\langle \hat{Q}_{20} \rangle}, \quad (6)$$

with $r_0 = 1.2 \text{ fm}$. The SCMF calculations are carried out in a harmonic oscillator basis, with the number of oscillator shells equal to 14.

Quadrupole collective states are obtained by solving the QCH, or the collective Schrödinger equation. The parameters of the QCH are completely determined by using the results of the RHB calculations: the quadrupole triaxial (β, γ) PES, and the single-particle solutions. More detailed accounts of the QCH are found, e.g., in Refs. [42, 44]. The QCH, denoted as \hat{H}_{coll} , is given as

$$\hat{H}_{\text{coll}} = \hat{T}_{\text{vib}} + \hat{T}_{\text{rot}} + V_{\text{coll}}, \quad (7)$$

with the vibrational kinetic energy

$$\begin{aligned} \hat{T}_{\text{vib}} = & -\frac{\hbar^2}{2\sqrt{wr}} \left[\frac{1}{\beta^4} \left(\frac{\partial}{\partial \beta} \sqrt{\frac{r}{w}} \beta^4 B_{\gamma\gamma} \frac{\partial}{\partial \beta} \right. \right. \\ & \left. \left. - \frac{\partial}{\partial \beta} \sqrt{\frac{r}{w}} \beta^3 B_{\beta\gamma} \frac{\partial}{\partial \gamma} \right) + \frac{1}{\beta \sin 3\gamma} \left(-\frac{\partial}{\partial \gamma} \sqrt{\frac{r}{w}} \sin 3\gamma \right. \right. \\ & \left. \left. \times B_{\beta\gamma} \frac{\partial}{\partial \beta} + \frac{1}{\beta} \frac{\partial}{\partial \gamma} \sqrt{\frac{r}{w}} \sin 3\gamma B_{\beta\beta} \frac{\partial}{\partial \gamma} \right) \right], \quad (8) \end{aligned}$$

rotational kinetic energy

$$\hat{T}_{\text{rot}} = \frac{1}{2} \sum_{k=1}^3 \frac{\hat{J}_k^2}{\mathcal{I}_k}, \quad (9)$$

and collective potential $V_{\text{coll}}(\beta, \gamma)$. Note that the operator \hat{J}_k in Eq. (9) denotes the components of the angular momentum in the body-fixed frame of a nucleus. The mass parameters $B_{\beta\beta}$, $B_{\beta\gamma}$, and $B_{\gamma\gamma}$ in Eq. (8) and the moments of inertia (denoted as MOIs) \mathcal{I}_k in (9) are functions of the β and γ deformations, and are related to each other by the quantity $\mathcal{I}_k = 4B_k \beta^2 \sin^2(\gamma - 2k\pi/3)$. Two additional quantities in Eq. (8), i.e., $r = B_1 B_2 B_3$, and $w = B_{\beta\beta} B_{\gamma\gamma} - B_{\beta\gamma}^2$, determine the volume element in the collective space. The moments of inertia are computed using the Inglis-Belyaev (IB) formula [63, 64], and the mass parameters are calculated in the cranking approximation. A well-known fact is that the IB formula considerably underestimates the empirical moments of inertia, and in order to account for the discrepancy it is often increased as

$$\mathcal{I}'_k = (1 + \alpha) \mathcal{I}_k, \quad (10)$$

with the scaling factor being typically 0.3–0.4 in literature. In this study, we scale the IB moment of inertia with a factor $\alpha = 0.3$ for all the Te nuclei.

The collective potential $V_{\text{coll}}(\beta, \gamma)$ (7) is obtained by subtracting the zero-point energy corrections from the total RHB deformation energy.

The corresponding eigenvalue problem is solved using an expansion of eigenfunctions in terms of a complete set of basis functions that depend on the deformation variables β and γ , and the three Euler angles. The diagonalization of the QCH with the ingredients specified by the RHB-SCMF calculation yields the excitation energies and collective wave functions for each value of the total angular momentum and parity, that are used to calculate various physical observables. A virtue of using the QCH based on SCMF single-(quasi)particle solutions is the fact that the electromagnetic transition properties, such as the electric quadrupole ($E2$) and monopole ($E0$) transition rates, and spectroscopic quadrupole moments, are calculated in the full configuration space, hence there is no need for effective charges. Using the bare value of the proton charge in the electric transition operators, the transition probabilities between eigenvectors of the QCH can be directly compared with spectroscopic data.

III. MEAN-FIELD RESULTS

A. Potential energy surfaces

Figure 1 shows the quadrupole triaxial PESs for the studied even-even $^{104-132}\text{Te}$ isotopes calculated by the constrained SCMF method within the RHB model that is based on the DD-PC1 EDF and separable pairing interaction (1) described in the previous section. As can be seen in Fig. 1, for light Te isotopes, $^{104-110}\text{Te}$, with the neutron numbers $N = 52 - 58$, the potential has the absolute minimum on the prolate axis around $\beta = 0.15$. For those Te nuclei heavier than ^{110}Te , the PES becomes considerably softer in γ deformation, indicating the strong shape mixing with respect to the nonaxial quadrupole deformation. A notably γ -soft energy surface with a shallow oblate global minimum at $\beta \approx 0.15$ is obtained for the ^{114}Te nucleus. In addition to the global minimum on the oblate side, a nearly prolate, triaxial local minimum becomes visible in the $^{116,118,120}\text{Te}$ nuclei. This points to the onset of the oblate-prolate shape coexistence toward the middle of the neutron major shell, i.e., $N = 66$. From ^{122}Te and the heavier Te nuclei, however, the local minimum on the prolate side diminishes, and only a weakly oblate deformed ground state is suggested. Approaching ^{130}Te , the minimum shifts to the spherical configuration, $\beta = 0$, reflecting the neutron shell closure $N = 82$.

The non-relativistic Gogny Hartree-Fock-Bogoliubov (HFB) calculation using the D1S force [28, 29] predicts a similar systematic behavior of the intrinsic shape along the Te isotopic chain. A major difference between the present and the Gogny-HFB calculations is that the latter gives the global mean-field minimum on the prolate side for $^{116,118,120}\text{Te}$, and both the prolate global minimum and oblate local minimum for these nuclei are quite

close in energy. The present calculation, however, predicts an oblate global minimum, along with the prolate local minimum, as mentioned above. The SCMF calculations have been reported in Ref. [24], which also adopted the RHB model but with the DD-ME2 EDF, in addition to the DD-PC1 EDF. In that work, mainly the systematic of the deformations and other intrinsic properties of the Te isotopic chain were studied, and the (β, γ) PESs obtained there for the Te nuclei are quite similar to those in the present calculation.

B. Single-particle energy spectra

In addition to the topology of the mean-field PES, the onset of deformation, especially that of shape coexistence, can be inferred from the behaviors of the single-particle spectra as functions of deformation, or Nilsson-like plots, which are obtained from the RHB calculation with the constraint on axial β deformation. Should a gap appear in the regions in which the density of the single-particle levels near the Fermi energies is low, it implies stability in nuclear structure at those nucleon numbers that are different from the spherical magic numbers. This situation is actually observed in Fig. 2, in which the proton and neutron single-particle energies near the Fermi energies are shown as functions of the axial quadrupole deformation β for ^{116}Te . At the mean-field level the oblate-prolate shape coexistence is particularly pronounced in this nucleus (cf. Fig. 1). In the proton single-particle spectra shown in Fig. 2(a), a large gap between the $\pi g_{7/2}$ and $\pi g_{9/2}$ orbitals at $\beta = 0$ represents the $Z = 50$ major shell closure. There is a region on the oblate ($\beta \approx -0.2$) side, in which level density near the proton Fermi energy is low. This can be related to the oblate ground state in the corresponding (β, γ) PES. In the neutron single-particle spectra, depicted in Fig. 2(b), one can notice a gap between the levels coming from the $\nu d_{3/2}$ and $\nu d_{5/2}$ single-particle orbitals, which is mainly extended to the oblate region $-0.2 \lesssim \beta \lesssim 0.1$. The neutron level density is also low at $\beta \approx 0.3$, which is created by the states originating from the $\nu h_{11/2}$, $\nu d_{3/2}$, $\nu d_{5/2}$, and $\nu g_{7/2}$ spherical single-particle states. The appearance of the gap in the neutron single-particle plot around the region $\beta \approx 0.3$ near the Fermi energy then implies that the prolate local minimum may occur as a consequence of the lowering of the intruding orbitals from the spherical $\nu h_{11/2}$ orbital. A similar, but much less pronounced gap on the prolate side is also visible in the proton single-particle spectra, which is formed by the lowering of the levels coming from the $\pi h_{11/2}$ orbital.

C. Dependencies on the pairing strength

We compare in Fig. 3 the PESs computed for ^{116}Te by using the default value of the pairing strength $V = 728$ MeV fm³ (left) and the increased strength $1.05V = 764$

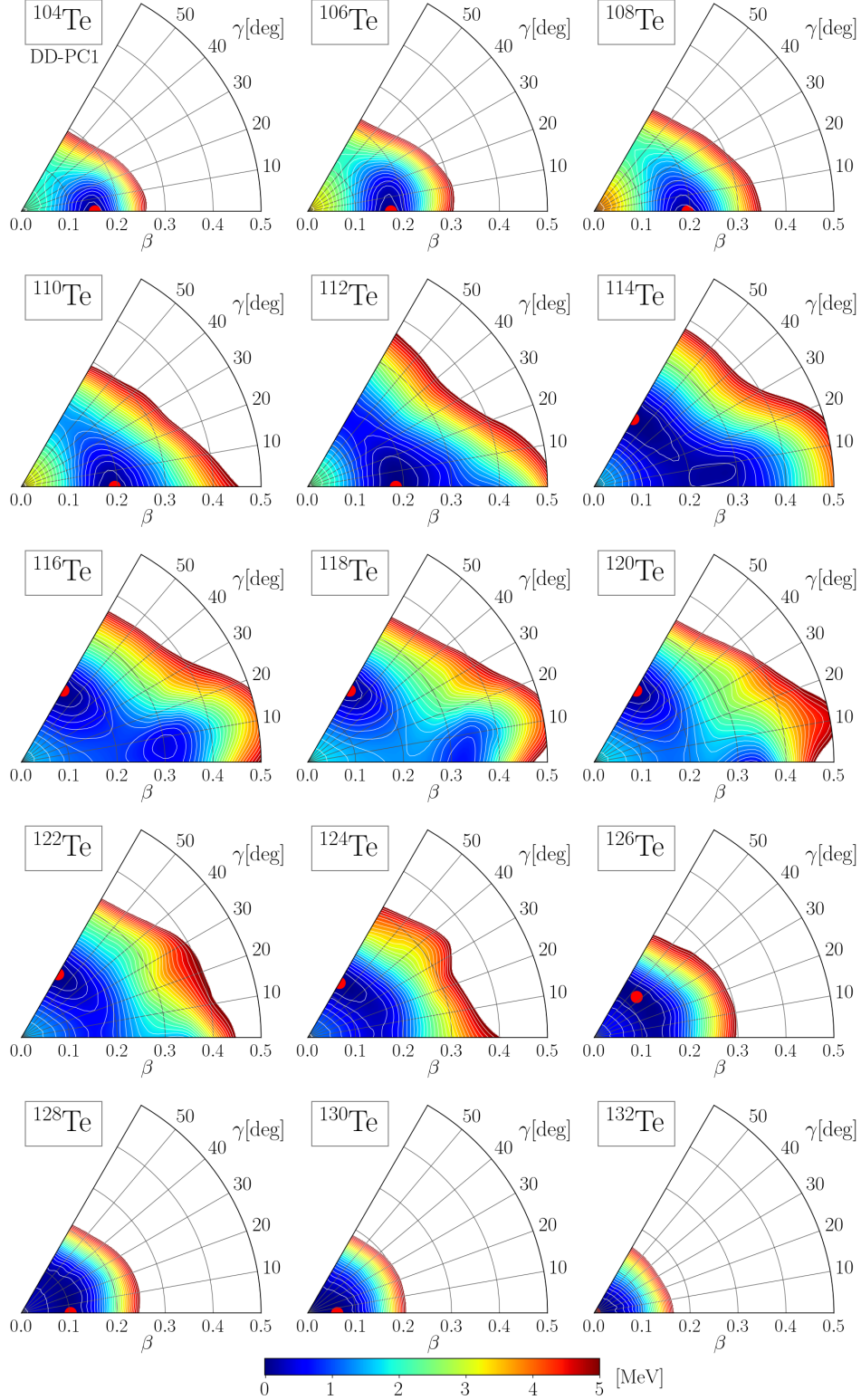


FIG. 1. Potential energy surfaces as functions of the triaxial quadrupole (β, γ) deformations for the even-even nuclei $^{104-132}\text{Te}$ computed with the constrained relativistic Hartree-Bogoliubov method employing the DD-PC1 energy density functional and the separable pairing force of finite range. The default pairing strength $V (f = 1.0)$ is used.

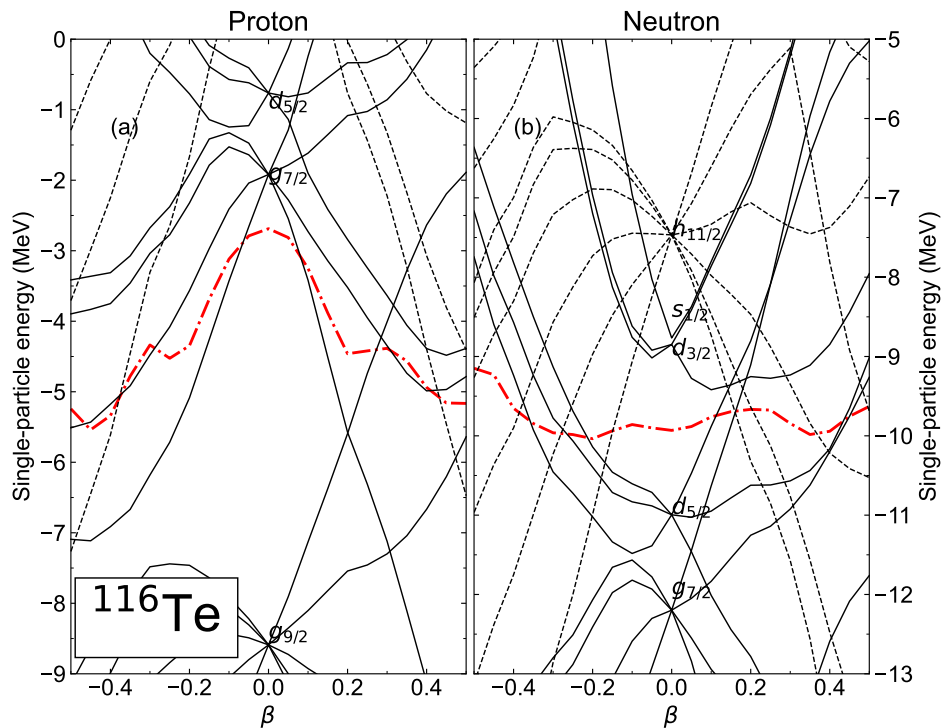


FIG. 2. Single-particle energies (in MeV) for protons (left) and neutrons (right) for ^{116}Te as functions of the axial quadrupole deformation β . The dashed-dotted curves stand for the Fermi energies.

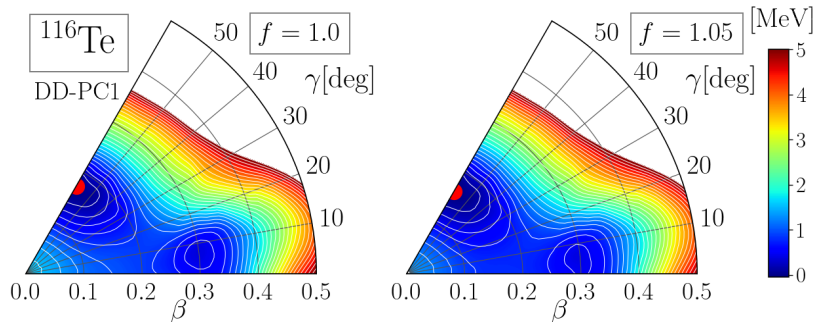


FIG. 3. (β, γ) PESs for ^{116}Te obtained from the RHB-SCMF calculations using the default pairing strength $V = 728 \text{ MeV fm}^3$ with a factor $f = 1.0$ (left), and the increased strength $1.05V = 764 \text{ MeV fm}^3$ with $f = 1.05$ (right). The DD-PC1 EDF is used.

MeV fm^3 (right), in the RHB-SCMF calculations based on the DD-PC1 EDF. For both nuclei, an impact of increasing the pairing strength in the RHB-SCMF calculation is such that the PES becomes softer in both β and γ deformations, and the prolate local minimum appears to be less pronounced in the calculation with the increased pairing strength. This reflects the fact that the pairing correlations rather prefer a less deformed nuclear shape. The increase of the pairing strength seems to have similar effects on the PESs for other Te nuclei, especially those near the mid-shell. The same is true when the DD-ME2 EDF is employed.

In addition to the potential energies, we study the sensitivity of the calculated pairing gaps to the pairing strength. Figure 4 shows the neutron and proton pairing gaps resulting from the RHB-SCMF calculations, performed at the (β, γ) coordinates corresponding to the global minimum, in the three different choices of the pairing strength with the scaling factors $f = 1.0$ (default value), $f = 1.05$, and $f = f(N)$ [see Eq. (3)]. $\Delta^{(5)}$ plotted in the figure represents the empirical pairing gap in the five-point formula, which is calculated by using the experimental binding energies available in Atomic Mass Evaluation 2020 (AME2020) [65, 66]. To compute pair-

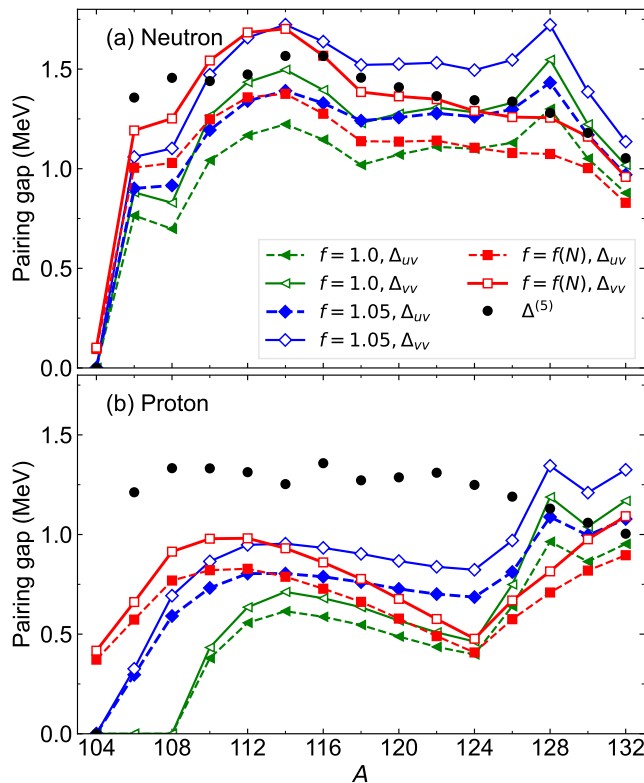


FIG. 4. Calculated (a) neutron and (b) proton pairing gaps Δ_{uv} (11) and Δ_{vv} (12) in the cases of the three different pairing strengths corresponding to the scaling factors $f = 1.0$, $f = 1.05$, and $f = f(N)$ [Eq. (3)] for the studied $^{104-132}\text{Te}$ nuclei. $\Delta^{(5)}$ represents the empirical pairing gap in the five-point formula calculated by using the experimental binding energies available at AME2020 [65, 66].

ing gaps we employ the following formulas that are often used in the literature:

$$\Delta_{uv} = \frac{\sum_k u_k v_k \Delta_k}{\sum_k u_k v_k} \quad (11)$$

and

$$\Delta_{vv} = \frac{\sum_k v_k^2 \Delta_k}{\sum_k v_k^2}, \quad (12)$$

where u_k and v_k are unoccupation and occupation amplitudes, respectively, Δ_k is the diagonal matrix element of the pairing field, and the sums in both equations run over all the considered states k in the canonical basis. See, e.g., Ref. [67], for the details about the above formulas.

We observe from Fig. 4(a) that the calculated neutron gap is rather sensitive to the pairing strength used in the RHB-SCMF model. This feature appears to hold regardless of which of the formulas Δ_{uv} and Δ_{vv} is employed, and is well illustrated by the fact that in Fig. 4(a) the calculated Δ 's with the scaling factor $f = 1.05$ are

systematically larger than those with the default pairing strength with $f = 1.0$ by typically 10–20 %. By using the N -dependent scaling factor for the neutron pairing strength, the corresponding pairing gap in each of the two formulas (11) and (12) turns out to be larger than that obtained with the default strength $f = 1.0$ on the neutron-deficient side ($A \leq 112$), but is reduced on the neutron-rich side ($A \geq 124$). Among all the calculated neutron pairing gaps shown in Fig. 4(a), the Δ_{vv} values calculated with the N -dependent scaling factor $f(N)$ are generally closest to the empirical neutron five-point pairing gaps, except perhaps for the $^{110,112,114}\text{Te}$ nuclei.

The calculated proton pairing gaps shown in Fig. 4(b) exhibit similar dependencies on the pairing strength to the neutron gaps, i.e., they increase (decrease) as the pairing strength is increased (decreased). As compared to the neutron gaps, the proton ones are predicted to be small since in most cases $\Delta < 1$, but are also sensitive to the pairing strength especially for the neutron-deficient nuclei. One can observe that the calculated proton pairing gaps significantly underestimate the empirical ones $\Delta^{(5)}$ for $A \lesssim 124$, and the disagreement becomes even more significant especially near the $N = 50$ neutron shell closure. This discrepancy is perhaps related to the fact that since the proton number $Z = 52$ of the Te isotopes is close to the magic number, where the occupation probabilities v^2 are close to either 0 or 1 near the Fermi surface, the formulas Δ_{uv} and Δ_{vv} do not necessarily give reasonable values. Another source of the discrepancy is that the same pairing strength is considered for both protons and neutrons in the present calculation, whereas the strength could be in principle different between the proton and neutron systems. To reproduce the empirical proton pairing gaps, the scaling factor for the proton pairing strength could be, for instance, much larger than the default value, $f \gg 1$, as one approaches the neutron-deficient side. The use of different pairing strengths for protons and neutrons would affect the spectroscopic results, but in order not to complicate the discussions we keep the equal neutron and proton pairing strengths in the present study.

IV. SPECTROSCOPIC RESULTS

A. Energy spectra

We show in Fig. 5 the calculated energy levels for the 2_1^+ , 4_1^+ , 0_2^+ , and 2_2^+ states using the RHB+QCH method in the case of the DD-PC1 EDF, and compare with the experimental data available from Ref. [17] and from the NNDC database [68]. In each panel of Fig. 5, different RHB+QCH results are depicted, obtained from the calculations that employ (i) the original pairing strength $f = 1.0$ and increased MOI with $\alpha = 0.3$, (ii) the pairing strength increased by 5 % ($f = 1.05$) and increased MOI with $\alpha = 0.3$, (iii) the nucleon-number dependent factor f (3) and increased MOI with $\alpha = 0.3$, and, as a

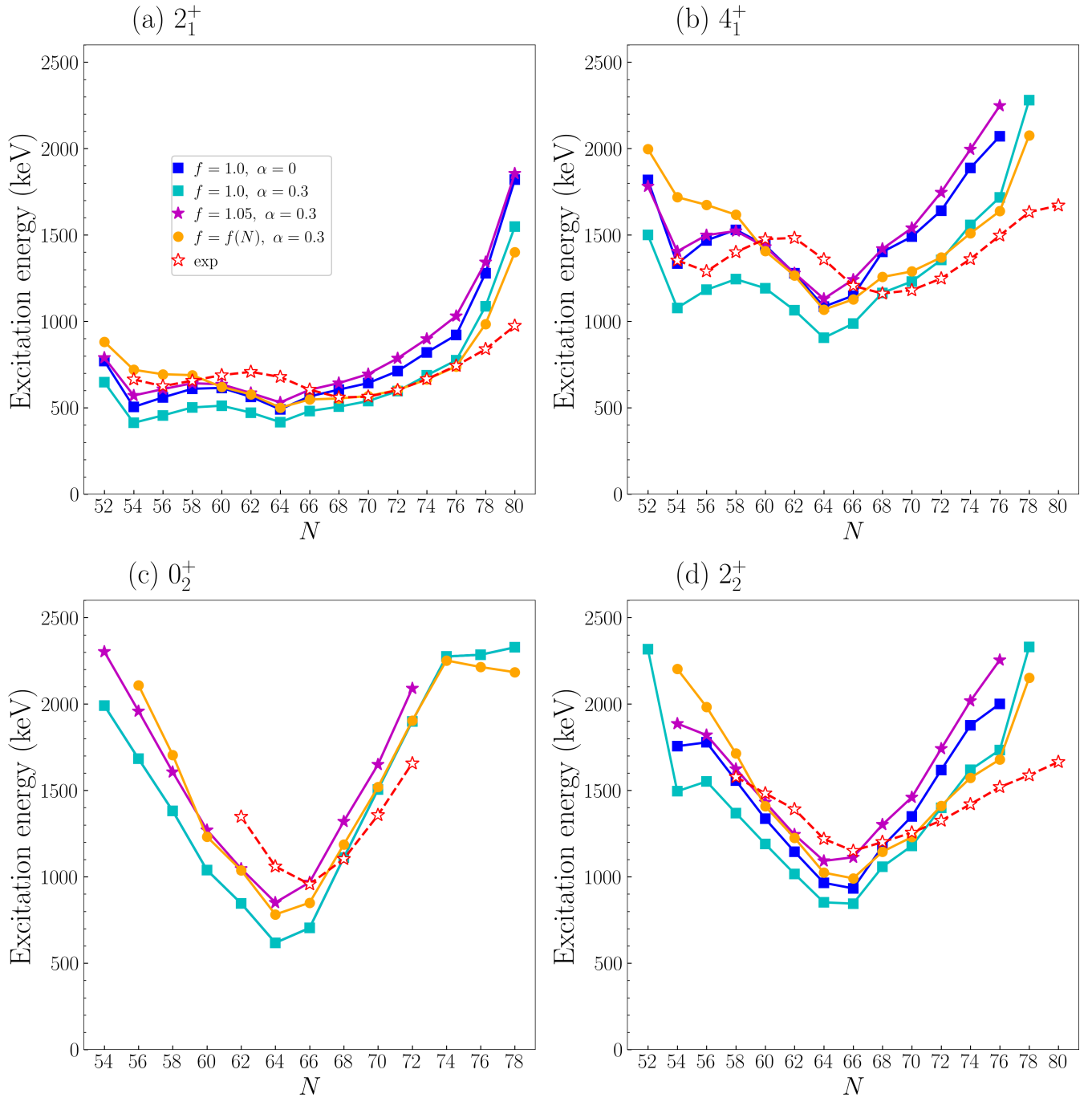


FIG. 5. Calculated excitation energies for the (a) 2_1^+ , (b) 4_1^+ , (c) 0_2^+ , and (d) 2_2^+ states predicted by the RHB+QCH model. The experimental data are taken from Refs. [17, 68]. The DD-PC1 EDF is employed. In each panel, the calculated energies using the (i) default pairing and MOI ($f = 1.0, \alpha = 0$), (ii) default pairing and increased MOI ($f = 1.0, \alpha = 0.3$), (iii) increased pairing and MOI ($f = 1.05, \alpha = 0.3$), and (iv) N -dependent [Eq. (3)] pairing strength and increased MOI [$f = f(N), \alpha = 0.3$] are shown.

reference, (iv) the original pairing ($f = 1.0$) as well as MOI ($\alpha = 0$). As a general remark, increasing the MOI has an effect of lowering the excitation energies of the states with spins other than 0^+ , while the energy levels of the excited 0^+ states remain the same. The increase

in the pairing strength makes the whole energy spectrum stretched.

In Figs. 5(a) and 5(b), it is seen that a characteristic behavior of the observed 2_1^+ and 4_1^+ energy levels as functions of the neutron number N is an approxi-

mate parabola that is found at $N = 56$ and 70 . The RHB+QCH calculations with the fixed pairing strengths (i.e., $f = 1.0$ and 1.05) for the entire isotopes provide similar systematic for the 2_1^+ and 4_1^+ levels, as they are lowest in energy at $N = 64$, and are locally minimal at $N = 54$. These neutron numbers are at variance with experiment. We note, however, that the EDF is usually not specifically adjusted to reproduce low-lying states along a given isotopic chain, and thus it is rather natural that the difference in a few nucleon numbers appears. The RHB+QCH predictions with the default pairing strength ($f = 1.0$) underestimate the 2_1^+ and 4_1^+ levels particularly for $N \leq 68$. For those nuclei with $70 \leq N \leq 76$, a reasonable description of the energy spectra is obtained with the increased ($\alpha = 0.3$) MOI. All the model calculations overestimate the observed 2_1^+ energies from $N > 76$ toward the neutron major shell closure $N = 82$. Note, however, that the collective model description becomes less reliable for those nuclei near the magic numbers, where single-particle degrees of freedom come to play a significant role.

The RHB+QCH calculations with the increased pairing with the fixed factor $f = 1.05$ and the MOI with $\alpha = 0.3$, produce the 2_1^+ and 4_1^+ yrast levels that are lying rather high in energy as compared to those calculations with the default pairing $f = 1.0$, and even higher excitation energies are obtained for $N \geq 68$ and as one approaches the $N = 82$ shell closure. To improve the description of the systematic for $N > 66$, it may be expected that the pairing strength should decrease as a function of N so that the energy levels are effectively lowered to be closer to the experimental ones. It is seen in Figs. 5(a) and 5(b) that the RHB+QCH calculation that employs the N -dependent pairing strength (3) does indeed give a slightly better description of the 2_1^+ systematic for $N \geq 66$ and $N \leq 58$. The same calculation, however, significantly overestimates the 4_1^+ energies for $N \leq 58$. This indicates that the employed pairing strengths for these nuclei may have been too large. It is worth mentioning that all the four RHB+QCH results give the 2_1^+ and 4_1^+ yrast levels for those nuclei with $N = 60 - 66$ that are lower than the experimental values. This is probably the consequence of the fact that the present RHB-SCMF calculation for the near mid-shell nuclei overestimates the quadrupole deformation, that is, the potential is so steep that the resulting collective energy spectrum becomes rather rotational like. For the mid-shell nuclei the RHB-SCMF also predicts coexisting minima and considerable shape mixing, rendering the low-spin (2_1^+) state unexpectedly lower in energy due to the level repulsion effect. Note that the Gogny-D1S HFB plus five-dimensional collective Hamiltonian (5DCH) calculation using the Gaussian overlap approximation [29] obtained the 2_1^+ excitation energies of 336 and 368 keV for ^{116}Te and ^{118}Te , respectively, which are close to the present results with the default pairing strength $f = 1.0$ and increased MOI ($\alpha = 0.3$), shown in Fig. 5(a).

In Fig. 5(c), experimentally the 0_2^+ energy level ex-

hibits a parabolic behavior with the minimal energy at the middle of the major shell $N = 66$. The nature of the 0_2^+ states in the near mid-shell Te nuclei has not yet been firmly identified. One explanation is that it belongs to the two-phonon multiplets of an anharmonic vibrator, since this state lies close in energy to the 4_1^+ and 2_2^+ levels. Alternative interpretation may be that it originates from the particle-hole excitation from below the $Z = 50$ proton major shell, which gives rise to a shape coexistence. The present RHB-QCH calculation seems to support the interpretation in terms of shape coexistence, based on the fact that an oblate global minimum and a well developed near prolate minimum appear in the triaxial quadrupole PESs (cf. Fig. 1). As shown in the next section, the calculated 0_2^+ states specifically for the $^{116,118}\text{Te}$ nuclei in the neutron mid-shell $N = 66$ are composed mainly of the mean-field configurations near the prolate secondary minimum. Overall, all the four RHB+QCH calculations give the 0_2^+ excitation energies that are systematically much lower than the experimental ones for the mid-shell Te nuclei. The RHB-SCMF PESs corresponding to these nuclei suggest that both the prolate local and oblate global minima are rather close in energy to each, and this may explain the unexpectedly low-energy 0_2^+ levels as compared to the experimental ones. In addition, the different calculations all suggest the lowest 0_2^+ energy to occur at $N = 64$, whereas experimentally the lowest 0_2^+ level is observed rather at $N = 66$. With the increased pairing strength with $f = 1.05$ and the N -dependent strength, the 0_2^+ level are pushed up. This change is most clearly seen for those nuclei with $N \leq 66$, where, for instance, a better agreement with data is observed for ^{118}Te when the pairing strength with $f = 1.05$ is employed. The calculation with the N -dependent pairing strength also gives a similar result for the 0_2^+ energy level systematic to that with the increased strength $f = 1.05$. The Gogny-D1S HFB plus 5DCH calculation of Ref. [29] obtained for ^{116}Te and ^{118}Te the 0_2^+ excitation energies of 755 and 750 keV, respectively, which are also similar to the present values.

Interpretation of the 2_2^+ state is not trivial in the present calculation, since as will be shown both $K^\pi = 0^+$ and 2^+ components are significantly mixed in this state. It may be considered a member of the two-phonon multiplets, the bandhead of the γ -vibrational band, or the member of the excited 0^+ band. The experimental systematic of this state, shown in Fig. 5(d), exhibits a parabolic pattern around $N = 66$, similarly to the 0_2^+ systematic. The present RHB+QCH calculations seem to produce a parabolic trend that is similar to the data, but the calculated 2_2^+ levels vary more rapidly with N for the region $N \geq 68$ than the experimental values.

Figure 6(a) summarizes the RHB-QCH results for the 2_1^+ , 4_1^+ , 0_2^+ , and 2_2^+ states obtained from the DD-PC1 EDF employing the N -dependent pairing strength. The QCH results in the case of the DD-ME2 EDF are also shown in Fig. 6(b). The results obtained from the DD-ME2 EDF are qualitatively similar to those from the DD-

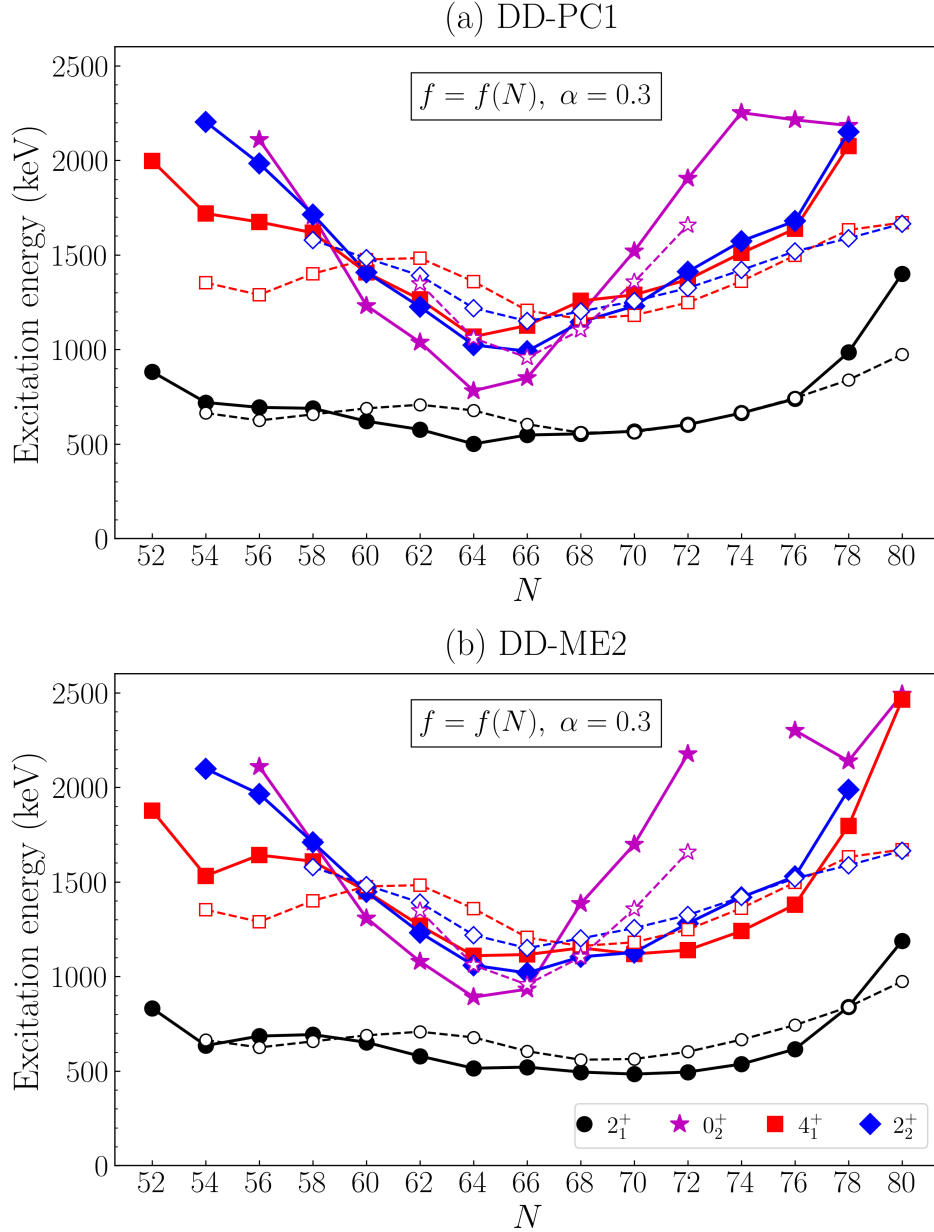


FIG. 6. Predicted low-energy spectra by the RHB+QCH model based on the (a) DD-PC1 and (b) DD-ME2 EDFs, represented by the solid symbols connected by solid lines. The corresponding experimental data [68] are shown as the open circles connected by broken lines. For both RHB-SCMF calculations, the N -dependent pairing strength $f(N)$ (3) is employed, and the MOI is scaled by 30 % ($\alpha = 0.3$).

PC1 EDF, a major difference being perhaps the location of the 0_2^+ energy level for the mid-shell nuclei with $62 \leq N \leq 66$. The RHB+QCH model employing the DD-ME2 EDF gives slightly higher lying 0_2^+ states than in the case of the DD-PC1 EDF. In addition, the DD-ME2 result exhibits slightly lower-lying 2_1^+ , 4_1^+ , and 2_2^+ levels on the neutron-deficient side than in the calculation with the DD-PC1 EDF. The results shown in Figs. 6(a) and 6(b) illustrate the difficulty in reproducing the 0_2^+ excitation energies in the mid-shell Te isotopes, irrespective of which

of the two representative relativistic EDFs is used for the RHB-SCMF calculation. We have also confirmed that increasing the pairing strength and rotational MOI does not appear to improve the description of the 0_2^+ levels in the case where the DD-ME2 functional is employed. The deficiency in reproducing the 0_2^+ energies in the mid-shell region with the QCH framework could be mainly attributed to the topology of their PESs, which exhibit two closely lying oblate global and prolate local minima. The topology of the PESs, in turn, depends much on

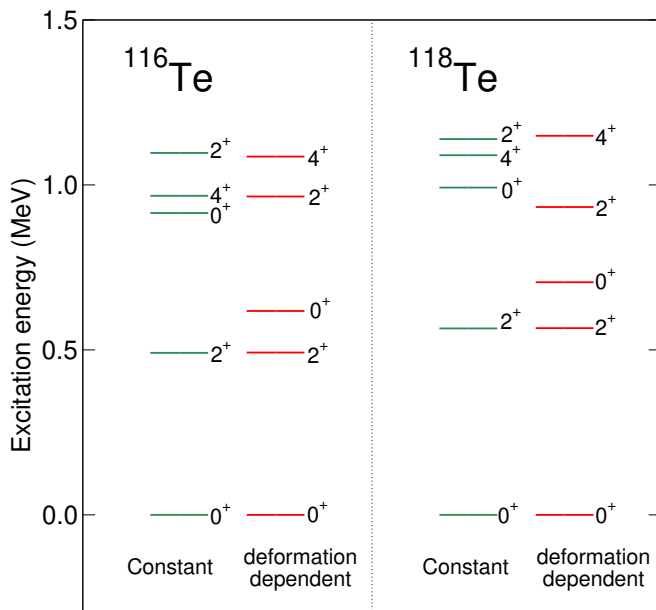


FIG. 7. Low-energy spectra for ^{116}Te and ^{118}Te obtained with the constant and deformation-dependent collective mass parameters. The MOI in the latter calculation is here not scaled (i.e., $\alpha = 0$), and the 2_1^+ energy in the former calculation is adjusted to that in the latter. The default pairing strength is employed in both calculations.

the properties of the underlying EDF in general, which is usually not specifically adjusted to particular nuclei under consideration.

We now try to identify which ingredients of the collective Hamiltonian make essential contributions to determine the low-energy level structure, especially, the location of the 0_2^+ energy level in the mid-shell Te isotopes. Here we specifically analyze the roles of the collective mass parameters, since they depend both on the β and γ deformations and are therefore influenced by the topology of the PES. In a recent QCH study using a Skyrme EDF [69], the QCH energy spectra calculated with the deformation-dependent rotational MOIs and vibrational mass parameters were compared with those obtained with constant mass parameters, and it was suggested that the deformation-dependent mass parameters play an important role in accurately predicting the properties of the excited 0^+ states in the $N \approx 28$ nuclei. Here we apply the above procedure to the studied Te nuclei, and perform additional RHB+QCH calculations with an assumption that all the mass parameters defined in Eqs. (8) and (9) should be constant and equal to each other, i.e., $B_1 = B_2 = B_3 = B_{\beta\beta} = B_{\gamma\gamma} \equiv B_0$, and that $B_{\beta\gamma} = 0$, as considered in Ref. [69].

Figure 7 compares between the RHB+QCH energy spectra for ^{116}Te and ^{118}Te , obtained with the constant and deformation-dependent mass parameters for the QCH. Note that, for the latter calculation, the original MOI ($\alpha = 0$) is used, and that the parameter B_0 in

the former calculation is determined to fit the 2_1^+ energy obtained from the former. In both calculations, the default pairing strength ($f = 1.0$) is employed. One can clearly see that for both $^{116,118}\text{Te}$ the 0_2^+ level obtained with the QCH employing the deformation-dependent collective mass parameters is substantially lower and closer in energy to the 2_1^+ one than that resulting from the QCH employing the constant mass parameters. This finding suggests that the deformation-dependent collective masses, which are influenced by the β as well as γ softness of the PES, make significant contributions to describe location of the excited 0_2^+ states relative to other states. A more thorough investigation on the effects of the mass parameters in a wider mass region within the relativistic EDF framework is an interesting future study.

Furthermore, a possible solution to improve description of the excited 0_2^+ levels would be to introduce additional collective coordinates to the triaxial quadrupole deformations, such as the dynamical pairing degree of freedom. The collective Hamiltonian that includes quadrupole deformations and dynamical pairing correlations was shown to provide a more accurate description of the excited 0^+ states and the bands built on them in the neighboring Xe isotopes and rare-earth nuclei with $N \approx 90$ [70–72].

As an alternative EDF-based approach to low-energy collective states, one could adopt the mapped IBM that explicitly takes into account configuration mixing between the normal and intruder states [73, 74]. Within this formalism, two independent IBM Hamiltonians, corresponding to the normal ($0p-0h$) and intruder ($2p-2h$) configurations, are determined by mapping the SCMF-PES onto the bosonic one, and are allowed to mix via certain mixing interactions (see Refs. [73, 74] for details). This procedure has been applied to a number of mass regions in which shape coexistence is suggested to occur [73–76], and would shed lights on the quality of the relativistic EDFs and the low-lying 0^+ states of the Te nuclei.

B. Collective wave functions

The nature of a given calculated state can be analyzed in terms of the collective wave function obtained as the eigenvector of the QCH at each deformation. Figures 8 and 9 show, respectively, distributions of the calculated collective wave functions for the 0_1^+ , 0_2^+ , 2_1^+ , 2_2^+ , 2_3^+ , and 4_1^+ states for the ^{116}Te and ^{118}Te nuclei. Here only the results obtained by using the default pairing strength with $f = 1.0$ in the RHB-SCMF calculation based on the DD-PC1 EDF and the default MOI with $\alpha = 0$ are considered without a loss of generality. Note that qualitatively very similar results are obtained from the calculations with the modified pairing strengths and/or MOI, and from those using the DD-ME2 EDF. For both ^{116}Te and ^{118}Te nuclei, the wave function for the 0_1^+ ground state is peaked at $\gamma \approx 36^\circ$, which corresponds to the oblate absolute minimum on the PES (see Fig. 1). The 0_1^+ wave func-

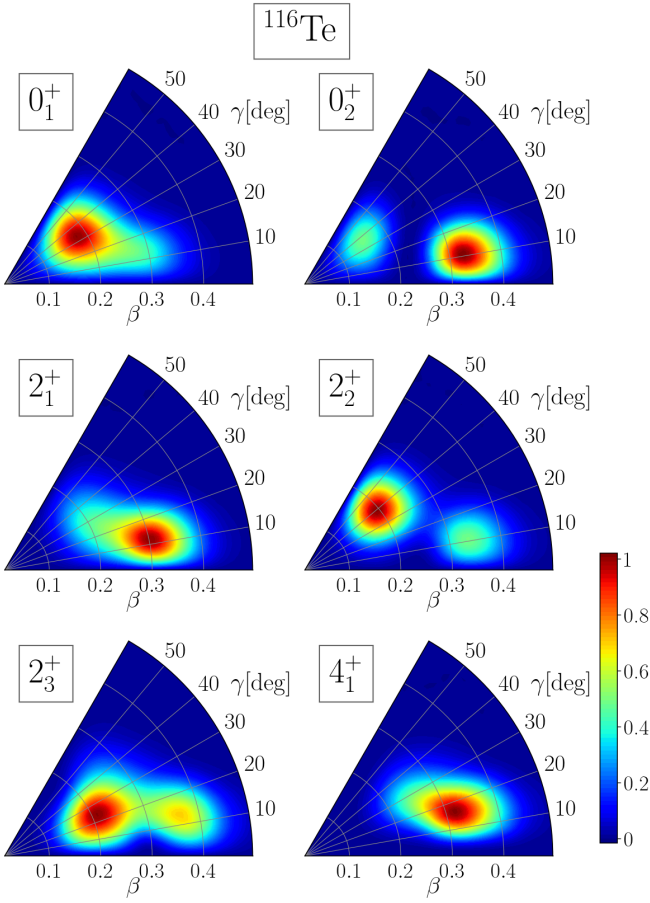


FIG. 8. Distributions of collective wave functions for the 0_1^+ , 0_2^+ , 2_1^+ , 2_2^+ , 2_3^+ , and 4_1^+ states in the (β, γ) plane of ^{116}Te , which are obtained from the RHB+QCH method using the default pairing strength V and MOI.

tion for the ^{116}Te is, however, more extended toward the prolate side within the range $0.2 \leq \beta \leq 0.3$, than that of ^{118}Te , and this implies strong shape mixing in the former nucleus. The 0_2^+ wave functions for both nuclei exhibit a distinct peak near the prolate axis, that is, $\gamma \approx 12^\circ$ and $\beta \approx 0.32$, which appears to be associated with the local minimum near the prolate axis in the PES. The fact that the distinct peaks appear, one on the oblate side in the 0_1^+ wave function and the other on the prolate side with larger β deformation in the 0_2^+ one, is in accordance with the presence of the closely lying oblate and prolate mean-field minima obtained in the RHB-SCMF calculation. From their collective wave functions, one could see that the ground state 0_1^+ can be here attributed to a near oblate triaxial deformation with β being ≈ 0.17 , while the 0_2^+ state is constructed based on the configurations representing a near prolate triaxial deformation with larger β (> 0.3) value.

As one can see in Figs. 8 and 9, the nature of the 2_1^+ collective wave function for the ^{116}Te nucleus is rather different from that of the ^{118}Te one: for the former the peak

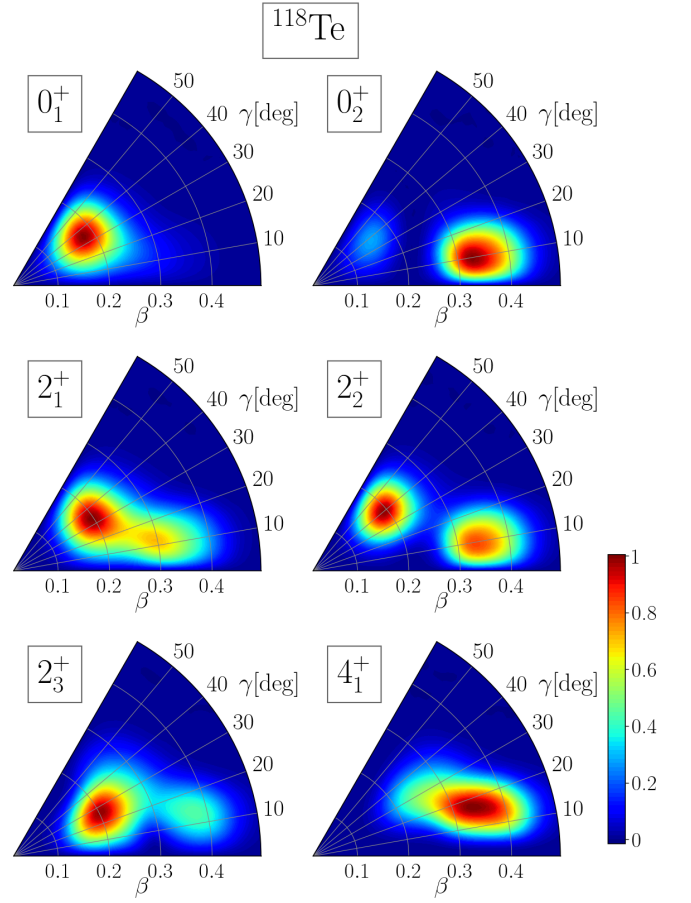


FIG. 9. Same as for Fig. 8, but for ^{118}Te .

is observed near the prolate axis with $(\beta, \gamma) \approx (0.3, 12^\circ)$, while for the latter a major peak is seen rather in the triaxial region, $(\beta, \gamma) \approx (0.2, 36^\circ)$, and a minor peak is also obtained near the prolate axis, $(\beta, \gamma) \approx (0.3, 10^\circ)$. The 2_1^+ as well as 0_2^+ states of ^{116}Te are, therefore, coming from the near prolate configurations that are supposed to originate from the intruder states. Concerning ^{118}Te , since the 0_1^+ and 2_1^+ wave functions are similar to each other in that both have a major peak in the triaxial oblate region, these states are supposed to be mostly composed of the weakly oblate deformed states, associated with the global oblate minimum in the corresponding PESs.

There are two peaks visible in the distributions of the 2_2^+ state for both Te nuclei, the major one in the triaxial oblate region and the other near the prolate axis. In addition, the peak on the prolate side in the 2_2^+ wave function distribution for ^{118}Te is higher than that of ^{116}Te , meaning that both triaxial oblate and prolate components are more strongly mixed in the 2_2^+ wave function for ^{118}Te than in the ^{116}Te counterpart.

The 2_3^+ collective wave functions for both ^{116}Te and ^{118}Te exhibit a major peak in the triaxial region with $\beta \approx 0.2$ and $\gamma \approx 25^\circ$, and a minor one near the prolate axis with $\beta \approx 0.37$ and $\gamma \approx 15^\circ$. These structures seem

to be more or less similar to those found in the 2_2^+ wave function distributions, which also exhibit two peaks on the oblate and prolate sides with slightly different (β, γ) coordinates. Given the distributions of the 2_2^+ and 2_3^+ collective wave functions, we find certain similarities between the structures of these two states.

For both ^{116}Te and ^{118}Te , the distribution of the calculated 4_1^+ collective wave function essentially has a single peak at $(\beta, \gamma) \approx (0.3 - 0.35, 15^\circ)$, and this suggests that the 4_1^+ state is mainly composed of the near prolate, triaxial configuration corresponding to the prolate local minimum on the mean-field PES. For the ^{116}Te nucleus, the 0_2^+ , 2_1^+ , and 4_1^+ collective wave functions exhibit a distinct peak on the prolate side, and this implies that these three states are, to a large extent, accounted for by the prolate deformed configurations.

C. Electric quadrupole and quadrupole properties

Figure 10 exhibits the calculated $B(E2; 2_1^+ \rightarrow 0_1^+)$, $B(E2; 4_1^+ \rightarrow 2_1^+)$, and $B(E2; 0_2^+ \rightarrow 2_1^+)$ values in Weisskopf units (W.u.), and $\rho^2(E0; 0_2^+ \rightarrow 0_1^+) \times 10^3$ values for the $^{104-132}\text{Te}$ isotopes as functions of the neutron number N . The four different RHB+QCH results with (i) $f = 1.0$ and $\alpha = 0$, (ii) $f = 1.0$ and $\alpha = 0.3$, (iii) $f = 1.05$ and $\alpha = 0.3$, and (iv) N -dependent f (3) and $\alpha = 0.3$ are compared, similarly to Fig. 5. Experimental data for the $B(E2)$ transition rates are available for ^{116}Te [17], ^{118}Te [16], ^{120}Te , and heavier Te nuclei [6, 68].

The predicted $B(E2; 2_1^+ \rightarrow 0_1^+)$, and $B(E2; 4_1^+ \rightarrow 2_1^+)$ values both monotonically increase toward the middle of the neutron major shell, $N = 64$ or 66 , reflecting the growing quadrupole collectivity in the open shell nuclei. The RHB+QCH calculation gives results that are larger than the measured $B(E2; 2_1^+ \rightarrow 0_1^+)$ values at $N = 66$ and 68 , while the agreement with experiment looks reasonable for $N \geq 70$. Concerning ^{116}Te , the present calculation provides the $B(E2; 2_1^+ \rightarrow 0_1^+)$ values of ≈ 50 W.u., which are within the error bar of the measured one [17], 33_{-10}^{+22} W.u. The $B(E2; 4_1^+ \rightarrow 2_1^+)$ value for the same nucleus is here calculated to be ≈ 115 W.u., while the recent measurement suggested the lower and upper limits of this transition rate to be 20 and 170 W.u., respectively. The phenomenological IBM-1 calculation assuming the single U(5) configuration, which was also reported in Ref. [17], provided the $B(E2; 2_1^+ \rightarrow 0_1^+)$ and $B(E2; 4_1^+ \rightarrow 2_1^+)$ values that are about half the ones obtained in the present calculation. All the four RHB+QCH calculations, shown in Figs. 10(a) and 10(b), appear to give essentially identical results.

The $B(E2; 0_2^+ \rightarrow 2_1^+)$ transition rate is considered an indicator of the shape mixing and coexistence. As seen from Fig. 10(c), the calculated values of this quantity near the mid-shell nuclei with $N = 60 - 66$ are generally large, and are almost in the same order of magnitude as the $B(E2; 4_1^+ \rightarrow 2_1^+)$ transition rates. This systematic corroborates the fact that substantial degree of softness

along the triaxial deformation is present in the mean-field PESs. The behavior of the predicted $B(E2; 4_1^+ \rightarrow 2_1^+)$ is further in accordance with the result that the 0_2^+ energy levels for these nuclei are calculated to be especially low. The RHB+QCH calculation suggests for the ^{116}Te nucleus the $0_2^+ \rightarrow 2_1^+$ $E2$ transition rate of 160 W.u., when the original pairing ($f = 1.0$) and MOI ($\alpha = 0$) are employed. An effect of increasing the MOI is such that the $B(E2; 0_2^+ \rightarrow 2_1^+)$ values are lowered for the $N = 64$ and 66 isotopes. With the increased MOI, the predicted $B(E2; 0_2^+ \rightarrow 2_1^+)$ values become lower, being closer to the upper limit of the measured value. Modification to the pairing strength, however, does not alter the $B(E2; 0_2^+ \rightarrow 2_1^+)$ transition rates. The corresponding experimental value for ^{116}Te available from [17] is 43_{-5}^{+6} W.u., which is much lower than the calculated values by a factor of 3 to 4. The enhanced $B(E2; 0_2^+ \rightarrow 2_1^+)$ transition rate illustrates that the present RHB+QCH calculation rather overestimates the degree of shape mixing for the near mid-shell Te nuclei, and this feature persists even if the increased pairing strength is employed in the RHB calculation.

The $E0$ transition between the 0_1^+ and 0_2^+ states is another signature of the shape mixing and evolution of collectivity. The predicted $\rho^2(E0; 0_2^+ \rightarrow 0_1^+) \times 10^3$ values, shown in Fig. 10, exhibit a monotonic increase toward the mid-shell, with the maximal value being found at $N = 64$. This appears to be a similar systematic behavior as a function of N to the $B(E2)$ values. Experimental information about the $E0$ transitions is scarce for Te isotopes, as only the available data are $\rho^2(E0; 0_2^+ \rightarrow 0_1^+) \times 10^3 = 13 \pm 6$ and 12 ± 3 for ^{118}Te and ^{124}Te , respectively [77]. The present calculation significantly overestimates these values. The calculated $\rho^2(E0; 0_2^+ \rightarrow 0_1^+) \times 10^3$ values for lighter Te near the neutron major shell $N = 50$ are, however, also large, even though the quadrupole collectivity is expected to be much less significant for near magic nuclei than in the open-shell nuclei. The $\rho^2(E0; 0_2^+ \rightarrow 0_1^+) \times 10^3$ values are here rather sensitive to the pairing strength, as it affects the energies and wave functions of the 0_2^+ states. The increase of the MOI does not change this transition at all, hence the results with the default and increased MOIs are identical in the plot.

D. Level scheme for ^{116}Te and ^{118}Te

We show in Figs. 11 and 12 the predicted low-energy level schemes for ^{116}Te and ^{118}Te . The calculated results are compared with the experimental data available from Refs. [17] and [16] for ^{116}Te and ^{118}Te , respectively. Note that the experimental level at 1637 keV is assigned to be the 3^+ state in the NNDC database [68], but in the new measurement of Ref. [17] it has been identified as the 2_3^+ state. The experimental level scheme shown on the right-hand side of Fig. 11 follows the latter assignment. The RHB+QCH results with the N -dependent pairing

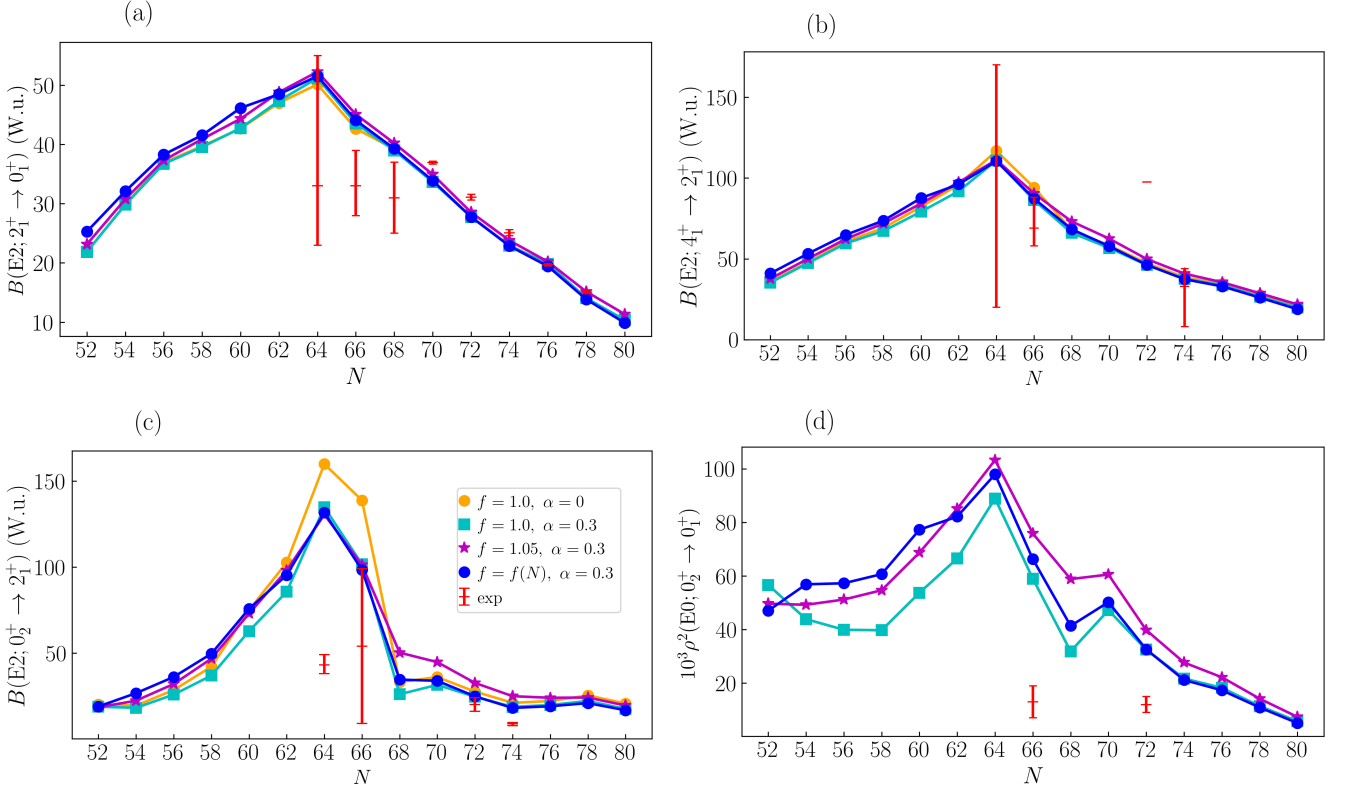


FIG. 10. (a) $B(E2; 2_1^+ \rightarrow 0_1^+)$, (b) $B(E2; 4_1^+ \rightarrow 2_1^+)$, and (c) $B(E2; 0_2^+ \rightarrow 2_1^+)$ values in Weisskopf units (W.u.), and (d) $\rho^2(E0; 0_2^+ \rightarrow 0_1^+) \times 10^3$ value for the $^{104-132}\text{Te}$ isotopes as functions of N , computed within the RHB+QCH method with the factor f for the pairing strength and the scaling factor α for the MOI equal to (i) $f = 1.0, \alpha = 0$, (ii) $f = 1.0, \alpha = 0.3$, (iii) $f = 1.05, \alpha = 0.3$, and (iv) $f = f(N), \alpha = 0.3$. The DD-PC1 EDF is used. Experimental $B(E2)$ values are taken from Ref. [17] for ^{116}Te , from Ref. [16] for ^{118}Te , and from Ref. [68] for all the other nuclei. The experimental $\rho^2(E0; 0_2^+ \rightarrow 0_1^+) \times 10^3$ values for ^{118}Te and ^{124}Te are taken from Ref. [77].

strength and increased MOI by 30 % are compared with those with the original pairing strength ($f = 1.0$) and MOI ($\alpha = 0$), and with the experimental data.

For ^{116}Te , both calculations provide similar results for the ground-state band, which look compressed as compared to the experimental one. The 0_2^+ level obtained with the modified pairing and MOI is closer to the measured one than with the original pairing and MOI. The 0_2^+ states is supposed to be the bandhead of the possible $K^\pi = 0_2^+$ band connected by dominant in-band $\Delta I = 2$ $E2$ transitions. In Fig. 11, the 2_2^+ level in both calculations is depicted as belonging to the 0_2^+ band, and the 2_3^+ as the bandhead of a band resembling γ -vibrational band connected by the $\Delta I = 1$ $E2$ transitions. As noted earlier, the $K^\pi = 0^+$ and $K^\pi = 2^+$ components are considerably mixed in the 2_2^+ and 2_3^+ states: 41 % and 59 % (56 % and 44 %) of the 2_2^+ (2_3^+) wave function is accounted for by the $K^\pi = 0^+$ and 2^+ components, respectively, in the case of the modified pairing and MOI. Similar degrees of K mixing in the 2_2^+ and 2_3^+ states are obtained from the calculation using the default pairing and MOI. The strong K mixing between the 2_2^+ and 2_3^+ states is also

evident from the fact that these states exhibit sizable $E2$ transitions to the 0_2^+ state, with the corresponding $B(E2)$ rates being 40 (35) W.u. and 23 (35) W.u., respectively, when the original pairing strength $f = 1.0$ [N -dependent strength $f(N)$] is used. Recall also that the distributions of the 2_2^+ and 2_3^+ collective wave functions in the (β, γ) plane (cf. Fig. 8) both exhibit a peak at the weak deformation $\beta \approx 0.2$ in triaxial region, and the other peak with larger $\beta > 0.3$ near the prolate axis. The 0_3^+ level is reproduced rather well by the RHB+QCH calculation, especially that with the modified pairing strength.

As it is seen in Fig. 12, basically similar level scheme to ^{116}Te is predicted for ^{118}Te . Overall, the calculated excitation energies for ^{118}Te agree with the experimental data [16] comparatively well. In particular, the predicted 0_2^+ energy level with the N -dependent pairing and increased MOI is higher than and closer to experimental counterpart than that with the default pairing and MOI.

Table I summarizes the calculated $B(E2)$ transition rates and electric quadrupole moments $Q(2^+)$ of low-energy states in ^{116}Te and ^{118}Te . The experimental data are taken from Ref. [17] for ^{116}Te , and Ref. [16] for

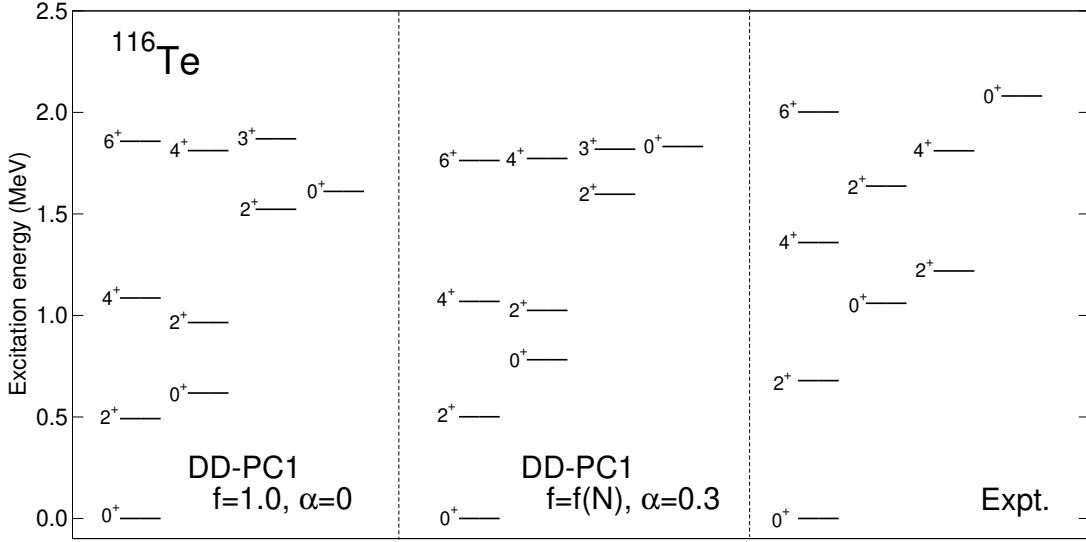


FIG. 11. Low-energy level scheme for ^{116}Te predicted by the RHB+QCH model using the DD-PC1 EDF and separable pairing force with (left) the default strength and the MOI, and (middle) the N -dependent pairing strength $f(N)$ and increased MOI with $\alpha = 0.3$. On the right-hand side shown are the experimental data [17].

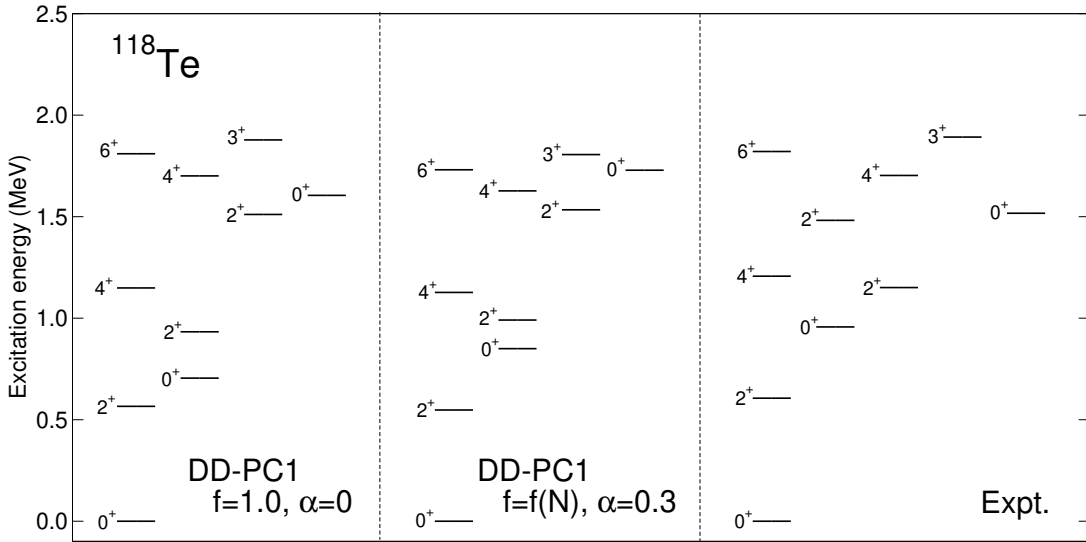


FIG. 12. Same as for Fig. 11, but for the ^{118}Te nucleus and the experimental data are taken from Ref. [16].

^{118}Te . The RHB+QCH calculation provides a substantially strong $B(E2; 0_2^+ \rightarrow 2_1^+)$ rate especially for ^{116}Te , which amounts to approximately by a factor of three larger than than the corresponding data. For the other $E2$ transitions of the non-yrast states, the QCH generally gives large $B(E2)$ rates, whereas the experimental information is rather limited for ^{116}Te as only the lower limits are known. More experimental $B(E2)$ data are available for the ^{118}Te nucleus. The RHB+QCH in most cases gives larger $B(E2)$'s than the experimental data, in particular, for the $6_1^+ \rightarrow 4_1^+$ and $0_2^+ \rightarrow 2_1^+$ $E2$ transitions. The calculation with the N -dependent pairing strength

with $f(N)$ and increased MOI gives the $B(E2; 0_2^+ \rightarrow 2_1^+)$ transition probability that is by 30 % lower than that obtained with the default pairing and MOI. The reduction is due to the change in the MOI. The experimental $B(E2; 6_1^+ \rightarrow 4_1^+)$ value that is in the same order of magnitude as the $B(E2; 4_1^+ \rightarrow 2_1^+)$ value seems to be an effect of configuration mixing. The present calculation is not able to account for this systematic.

Experimental information about the $Q(2^+)$ moments is not available for both nuclei, but the predicted values with the default (modified) pairing force, $Q(2_1^+) = -0.75$ (-0.62) eb and -0.42 (-0.25) eb for ^{116}Te and ^{118}Te ,

TABLE I. Calculated $B(E2)$ rates (in W.u.) and electric quadrupole moments $Q(2_{1,2}^+)$ (in eb) for the ^{116}Te and ^{118}Te nuclei, within the RHB+QCH calculations with the default pairing $f = 1.0$ and MOI $\alpha = 0$ (column 4, denoted as “default”), and with the N -dependent pairing strength $f = f(N)$ and increased MOI with $\alpha = 0.3$ (column 5, denoted as “modified”). The DD-PC1 EDF is employed. Experimental data for ^{116}Te and ^{118}Te are adopted from Refs. [17] and [16], respectively.

		Expt.	RHB+QCH	
			default	modified
^{116}Te	$B(E2; 2_1^+ \rightarrow 0_1^+)$	33_{-10}^{+22}	50	51
	$B(E2; 2_2^+ \rightarrow 0_1^+)$		2.5	1.1
	$B(E2; 2_2^+ \rightarrow 0_2^+)$		40	35
	$B(E2; 2_2^+ \rightarrow 2_1^+)$	41_{-5}^{+6}	55	69
	$B(E2; 2_3^+ \rightarrow 0_1^+)$		0.10	0.088
	$B(E2; 2_3^+ \rightarrow 0_2^+)$	> 20	23	35
	$B(E2; 2_3^+ \rightarrow 2_1^+)$	> 3	5.5	3.7
	$B(E2; 2_3^+ \rightarrow 2_2^+)$		36	32
	$B(E2; 3_1^+ \rightarrow 2_3^+)$		63	63
	$B(E2; 4_1^+ \rightarrow 2_1^+)$	> 20 and < 170	117	110
	$B(E2; 4_2^+ \rightarrow 2_1^+)$	> 0.7	1.5	2.4
	$B(E2; 4_2^+ \rightarrow 2_2^+)$	> 5	69	68
	$B(E2; 4_2^+ \rightarrow 4_1^+)$		24	35
	$B(E2; 6_1^+ \rightarrow 4_1^+)$	> 27	166	161
	$B(E2; 0_2^+ \rightarrow 2_1^+)$	43_{-5}^{+6}	160	132
	$B(E2; 0_3^+ \rightarrow 2_1^+)$		0.016	0.33
	$B(E2; 0_3^+ \rightarrow 2_2^+)$		65	68
	$B(E2; 0_3^+ \rightarrow 2_3^+)$		3.3	2.9
	$Q(2_1^+)$		-0.75	-0.62
	$Q(2_2^+)$		0.051	0.050
^{118}Te	$B(E2; 2_1^+ \rightarrow 0_1^+)$	33_{-5}^{+6}	43	44
	$B(E2; 2_2^+ \rightarrow 0_1^+)$	$1.8_{-0.4}^{+0.7}$	1.2	0.11
	$B(E2; 2_2^+ \rightarrow 0_2^+)$		62	56
	$B(E2; 2_2^+ \rightarrow 2_1^+)$	28_{-7}^{+13}	72	77
	$B(E2; 2_3^+ \rightarrow 0_1^+)$		0.025	0.011
	$B(E2; 2_3^+ \rightarrow 0_2^+)$	60_{-17}^{+35}	22	36
	$B(E2; 2_3^+ \rightarrow 2_1^+)$	$3.4_{-0.9}^{+1.9}$	13	10
	$B(E2; 2_3^+ \rightarrow 2_2^+)$	$9.5_{-3.5}^{+8.9}$	28	28
	$B(E2; 3_1^+ \rightarrow 2_3^+)$		61	59
	$B(E2; 4_1^+ \rightarrow 2_1^+)$	69_{-11}^{+19}	94	87
	$B(E2; 4_2^+ \rightarrow 2_1^+)$	< 1.1	7.9	5.2
	$B(E2; 4_2^+ \rightarrow 2_2^+)$	< 210	63	70
	$B(E2; 4_2^+ \rightarrow 4_1^+)$	< 160	27	43
	$B(E2; 6_1^+ \rightarrow 4_1^+)$	80_{-10}^{+14}	178	162
	$B(E2; 0_2^+ \rightarrow 2_1^+)$	54 ± 45	139	98
	$B(E2; 0_3^+ \rightarrow 2_1^+)$	1.3 ± 45	3.6	5.1
	$B(E2; 0_3^+ \rightarrow 2_2^+)$	100	52	59
	$Q(2_1^+)$		-0.42	-0.25
	$Q(2_2^+)$		-0.37	-0.40

respectively, are similar to the observed ones, both in magnitude and sign, for the heavier Te isotopes [78].

V. SUMMARY

Evolution and coexistence of the intrinsic shape and the corresponding collective excitations in the even-even $^{104-132}\text{Te}$ isotopes have been investigated using the theoretical framework of the relativistic EDF. The starting point of the present analysis was the constrained RHB-SCMF calculations that employ the DD-PC1 and DD-ME2 EDFs, and the separable pairing force of finite range. By using as a microscopic input the SCMF solutions, the deformation-dependent mass parameters and moments of inertia, and collective potential have been completely determined.

We found in the resultant quadrupole triaxial (β, γ) PESs for the near mid-shell nuclei, $^{114-120}\text{Te}$, coexisting two minima that appear close in energy to each other: a weakly deformed oblate global minimum and a strongly deformed triaxial local minimum near the prolate ($\gamma = 0^\circ$) axis. The calculated 0_2^+ level has been shown to exhibit a parabolic behavior as a function of N , which is considered a signature of shape coexistence as expected empirically. The present RHB+QCH calculation, however, has yielded for the mid-shell Te nuclei significantly low-energy 0_2^+ levels as compared to the experimental ones. The description of the 0_2^+ excitation energies in the mid-shell region is supposed to be, to a large extent, sensitive to the topology of the (β, γ) PESs, that is, the presence of the two closely lying oblate global and prolate local mean-field minima. These characteristics of the PESs, in turn, reflect the nature of the underlying EDF. The calculated $B(E2)$ and $\rho^2(E0)$ values also served as an indicator for the shape coexistence as well as growing quadrupole collectivity toward the neutron mid-shell $N = 66$. Here the $B(E2; 0_2^+ \rightarrow 2_1^+)$ and $\rho^2(E0; 0_2^+ \rightarrow 0_1^+)$ values for the mid-shell Te nuclei with $N \approx 64$ have been calculated to be too large, as compared with the available data, probably because a substantial degree of shape mixing occurs in the model calculation due to the softness in both β and γ deformations.

We have also studied the sensitivity of the spectroscopic results to the pairing strength employed in the RHB-SCMF calculation. It was shown that by increasing the pairing strength energy levels of the excited states were systematically raised, while the excitation energies for those nuclei with $N \geq 68$ were predicted to be even higher than the experimental ones as the $N = 82$ major shell closure is approached. By using the N -dependent scaling factor for the pairing strength, certain improvements of the RHB+QCH description have been made, especially on the neutron-rich side. In addition, the deformation-dependent mass parameters in the collective Hamiltonian were shown to make an important contribution to determine the location of the 0_2^+ energy level relative to the 2_1^+ one of the near mid-shell nuclei $^{116,118}\text{Te}$. These mass parameters reflect the topology of their PESs, which exhibit two minima and pronounced γ softness in the case of ^{116}Te .

The present study suggests a coexistence of an oblate

and a near prolate shapes in mid-shell Te isotopes, as expected experimentally, and provides theoretical predictions on these nuclei which are experimentally of much interest. From the theoretical point of view, the deficiency of the employed model in describing the correct location of the 0_2^+ level in the mid-shell region stimulates further theoretical investigations to reveal possible sources of the uncertainties, which are in the present case rooted in the

nature of the EDF, the SCMF method, the parameters or the degrees of freedom involved in the QCH.

ACKNOWLEDGMENTS

The authors thank Kenichi Yoshida for a valuable discussion.

-
- [1] A. Bohr and B. R. Mottelson, *Nuclear Structure*, Vol. II (Benjamin, New York, USA, 1975).
- [2] P. Cejnar, J. Jolie, and R. F. Casten, *Rev. Mod. Phys.* **82**, 2155 (2010).
- [3] K. Heyde, C. De Coster, J. Jolie, and J. L. Wood, *Phys. Rev. C* **46**, 541 (1992).
- [4] J. L. Wood, K. Heyde, W. Nazarewicz, M. Huyse, and P. van Duppen, *Phys. Rep.* **215**, 101 (1992).
- [5] K. Heyde and J. L. Wood, *Rev. Mod. Phys.* **83**, 1467 (2011).
- [6] P. E. Garrett, M. Zielińska, and E. Clément, *Prog. Part. Nucl. Phys.* **124**, 103931 (2022).
- [7] H. Morinaga, *Phys. Rev.* **101**, 254 (1956).
- [8] A. N. Andreyev, M. Huyse, P. Van Duppen, L. Weissman, D. Ackermann, J. Gerl, F. P. Hessberger, S. Hofmann, A. Kleinböhl, G. Münzenberg, S. Reshitko, C. Schlegel, H. Schaffner, P. Cagarda, M. Matos, S. Saro, A. Keenan, C. Moore, C. D. O'Leary, R. D. Page, M. Taylor, H. Ketunen, M. Leino, A. Lavrentiev, R. Wyss, and K. Heyde, *Nature (London)* **405**, 430 (2000).
- [9] P. Federman and S. Pittel, *Phys. Lett. B* **69**, 385 (1977).
- [10] K. Heyde, P. Van Isacker, R. F. Casten, and J. L. Wood, *Phys. Lett. B* **155**, 303 (1985).
- [11] K. Heyde, J. Jolie, H. Lehmann, C. De Coster, and J. Wood, *Nucl. Phys. A* **586**, 1 (1995).
- [12] R. Bengtsson, T. Bengtsson, J. Dudek, G. Leander, W. Nazarewicz, and J. ye Zhang, *Phys. Lett. B* **183**, 1 (1987).
- [13] R. Bengtsson and W. Nazarewicz, *Z. Phys. A* **334**, 269 (1989).
- [14] S. Ćwiok, P. H. Heenen, and W. Nazarewicz, *Nature* **433**, 705 (2005).
- [15] J. Rikovska, N. Stone, P. Walker, and W. Walters, *Nuclear Physics A* **505**, 145 (1989).
- [16] C. Mihai, A. A. Pasternak, S. Pascu, D. Filipescu, M. Ivaşcu, D. Bucureşcu, G. C ăta Danil, I. C ăta Danil, D. Deleanu, D. G. Ghiţă, T. Glodariu, N. Mărginean, R. Mărginean, A. Negret, T. Sava, L. Stroe, G. Suliman, and N. V. Zamfir, *Phys. Rev. C* **83**, 054310 (2011).
- [17] F. von Spee, M. Beckers, A. Blazhev, A. Dewald, F. Dunkel, A. Esmaylzadeh, C. Fransen, G. Hackenberg, J. Jolie, L. Knafla, C.-D. Lakenbrink, M. Schiffer, N. Warr, and M. Weinert, *Phys. Rev. C* **109**, 024325 (2024).
- [18] F. Iachello and A. Arima, *The interacting boson model* (Cambridge University Press, Cambridge, 1987).
- [19] E. A. Cederlöf, T. Bäck, J. Nyberg, C. Qi, A. Ataç, H. Badran, T. Braunroth, T. Calverley, D. M. Cox, M. Doncel, T. Grahn, P. Greenlees, J. Hilton, R. Julin, S. Juutinen, J. Konki, H. Li, S. Matta, V. Modamio, B. S. N. Singh, J. Pakarinen, P. Papadakis, J. Partanen, P. Rakhila, P. Ruotsalainen, M. Sandzelius, J. Sarén, C. Scholey, S. Stolze, P. Subramaniam, J. Uusitalo, and J. J. Valiente-Dobón, *The European Physical Journal A* **59**, 300 (2023).
- [20] C. B. Li, Y. Zheng, T. X. Li, X. G. Wu, H. Y. Wu, M. Zheng, Z. H. Zhao, Y. Q. Li, R. Hong, Z. Y. He, J. Z. Li, J. L. Wang, C. Y. Guo, Z. X. Zhou, L. Ni, G. S. Li, X. H. Zhou, B. Guo, S. Y. Wang, M. L. Liu, Y. H. Zhang, C. Y. He, F. L. Liu, S. Wang, and L. H. Zhu, *Phys. Rev. C* **109**, 034310 (2024).
- [21] C. Qi, *Phys. Rev. C* **94**, 034310 (2016).
- [22] K. Kaneko, N. Shimizu, T. Mizusaki, and Y. Sun, *Phys. Rev. C* **103**, L021301 (2021).
- [23] S. Sharma, R. Devi, and S. K. Khosa, *Int. J. Mod. Phys. E* **31**, 2250053 (2022), <https://doi.org/10.1142/S0218301322500537>.
- [24] S. Sharma, R. Devi, and S. Khosa, *Nuclear Physics A* **988**, 9 (2019).
- [25] D. Bonatsos, K. E. Karakatsanis, A. Martinou, T. J. Mertzimekis, and N. Minkov, *Phys. Rev. C* **106**, 044323 (2022).
- [26] L. Próchniak, K. Zajac, K. Pomorski, S. Rohoziński, and J. Srebrny, *Nucl. Phys. A* **648**, 181 (1999).
- [27] J. Libert, B. Roussière, and J. Sauvage, *Nuclear Physics A* **786**, 47 (2007).
- [28] J. P. Delaroche, M. Girod, J. Libert, H. Goutte, S. Hilaire, S. Péru, N. Pillet, and G. F. Bertsch, *Phys. Rev. C* **81**, 014303 (2010).
- [29] http://www-phynu.cea.fr/science_en_ligne/carte_potentiels_microscopiques/carte_potentiel_nucleaire_eng.htm.
- [30] M. Sambataro, *Nuclear Physics A* **380**, 365 (1982).
- [31] H. Lehmann, J. Jolie, C. De Coster, B. Decroix, K. Heyde, and J. L. Wood, *Nucl. Phys. A* **621**, 767 (1997).
- [32] S. Pascu, N. V. Zamfir, G. C ăta Danil, and N. Mărginean, *Phys. Rev. C* **81**, 054321 (2010).
- [33] J. B. Gupta, *Phys. Rev. C* **107**, 034315 (2023).
- [34] R. Budaca and A. I. Budaca, *The European Physical Journal Plus* **136**, 983 (2021).
- [35] E. A. Coello Pérez and T. Papenbrock, *Phys. Rev. C* **92**, 064309 (2015).
- [36] T. H. R. Skyrme, *Nucl. Phys.* **9**, 615 (1958).
- [37] M. Bender, P.-H. Heenen, and P.-G. Reinhard, *Rev. Mod. Phys.* **75**, 121 (2003).
- [38] N. Schunck, ed., *Energy Density Functional Methods for Atomic Nuclei* (IOP Publishing, 2019).
- [39] J. Decharge and M. Girod and D. Gogny, *Phys. Lett. B* **55**, 361 (1975).

- [40] L. M. Robledo, T. R. Rodríguez, and R. R. Rodríguez-Guzmán, *J. Phys. G: Nucl. Part. Phys.* **46**, 013001 (2019).
- [41] D. Vretenar, A. V. Afanasjev, G. A. Lalazissis, and P. Ring, *Phys. Rep.* **409**, 101 (2005).
- [42] T. Nikšić, D. Vretenar, and P. Ring, *Prog. Part. Nucl. Phys.* **66**, 519 (2011).
- [43] P. Ring and P. Schuck, *The Nuclear Many-Body Problem* (Springer-Verlag, Berlin, 1980).
- [44] T. Nikšić, Z. P. Li, D. Vretenar, L. Próchniak, J. Meng, and P. Ring, *Phys. Rev. C* **79**, 034303 (2009).
- [45] K. Nomura, N. Shimizu, and T. Otsuka, *Phys. Rev. Lett.* **101**, 142501 (2008).
- [46] K. Nomura, N. Shimizu, and T. Otsuka, *Phys. Rev. C* **81**, 044307 (2010).
- [47] K. Nomura, T. Otsuka, N. Shimizu, and L. Guo, *Phys. Rev. C* **83**, 041302 (2011).
- [48] Z. P. Li, T. Nikšić, D. Vretenar, J. Meng, G. A. Lalazissis, and P. Ring, *Phys. Rev. C* **79**, 054301 (2009).
- [49] Z. P. Li, T. Nikšić, and D. Vretenar, *J. Phys. G: Nucl. Part. Phys.* **43**, 024005 (2016).
- [50] J. Xiang, Z. P. Li, W. H. Long, T. Nikšić, and D. Vretenar, *Phys. Rev. C* **98**, 054308 (2018).
- [51] X. Q. Yang, L. J. Wang, J. Xiang, X. Y. Wu, and Z. P. Li, *Phys. Rev. C* **103**, 054321 (2021).
- [52] K. Nomura and K. E. Karakatsanis, *Phys. Rev. C* **106**, 064317 (2022).
- [53] Z. P. Li, J. M. Yao, D. Vretenar, T. Nikšić, H. Chen, and J. Meng, *Phys. Rev. C* **84**, 054304 (2011).
- [54] V. Prassa, T. Nikšić, G. A. Lalazissis, and D. Vretenar, *Phys. Rev. C* **86**, 024317 (2012).
- [55] K. E. Karakatsanis and K. Nomura, *Phys. Rev. C* **105**, 064310 (2022).
- [56] T. Nikšić, N. Paar, D. Vretenar, and P. Ring, *Comput. Phys. Commun.* **185**, 1808 (2014).
- [57] A. Bjelčić, T. Nikšić, and Z. Drmač, DIRHBSpeedup, <https://github.com/abjelcic/DIRHBSpeedup.git> (2021).
- [58] T. Nikšić, D. Vretenar, and P. Ring, *Phys. Rev. C* **78**, 034318 (2008).
- [59] G. A. Lalazissis, T. Nikšić, D. Vretenar, and P. Ring, *Phys. Rev. C* **71**, 024312 (2005).
- [60] Y. Tian, Z. Y. Ma, and P. Ring, *Phys. Lett. B* **676**, 44 (2009).
- [61] J. F. Berger, M. Girod, and D. Gogny, *Nucl. Phys. A* **428**, 23 (1984).
- [62] S. Teeti and A. V. Afanasjev, *Phys. Rev. C* **103**, 034310 (2021).
- [63] D. R. Inglis, *Phys. Rev.* **103**, 1786 (1956).
- [64] S. Beliaev, *Nucl. Phys.* **24**, 322 (1961).
- [65] W. Huang, M. Wang, F. Kondev, G. Audi, and S. Naimi, *Chinese Physics C* **45**, 030002 (2021).
- [66] M. Wang, W. Huang, F. Kondev, G. Audi, and S. Naimi, *Chinese Physics C* **45**, 030003 (2021).
- [67] S. E. Agbemava, A. V. Afanasjev, D. Ray, and P. Ring, *Phys. Rev. C* **89**, 054320 (2014).
- [68] Brookhaven National Nuclear Data Center, <http://www.nndc.bnl.gov>.
- [69] K. Washiyama and K. Yoshida, *Phys. Rev. C* **108**, 014323 (2023).
- [70] J. Xiang, Z. P. Li, T. Nikšić, D. Vretenar, and W. H. Long, *Phys. Rev. C* **101**, 064301 (2020).
- [71] K. Nomura, D. Vretenar, Z. P. Li, and J. Xiang, *Phys. Rev. C* **102**, 054313 (2020).
- [72] J. Xiang, Z. P. Li, T. Nikšić, D. Vretenar, W. H. Long, and X. Y. Wu, *Phys. Rev. C* **109**, 044319 (2024).
- [73] K. Nomura, R. Rodríguez-Guzmán, L. M. Robledo, and N. Shimizu, *Phys. Rev. C* **86**, 034322 (2012).
- [74] K. Nomura, T. Otsuka, and P. Van Isacker, *Journal of Physics G: Nuclear and Particle Physics* **43**, 024008 (2016).
- [75] K. Nomura, R. Rodríguez-Guzmán, and L. M. Robledo, *Phys. Rev. C* **87**, 064313 (2013).
- [76] K. Nomura, R. Rodríguez-Guzmán, and L. M. Robledo, *Phys. Rev. C* **94**, 044314 (2016).
- [77] T. Kibédi and R. Spear, *At. Data and Nucl. Data Tables* **89**, 77 (2005).
- [78] N. Stone, *At. Data Nucl. Data Tables* **90**, 75 (2005).